Simulation of the Tropical Pacific Climate with a Coupled Ocean–Atmosphere General Circulation Model. Part I: The Seasonal Cycle

A. W. ROBERTSON,* C.-C. MA, C. R. MECHOSO, AND M. GHIL*

Department of Atmospheric Sciences, University of California at Los Angeles, Los Angeles, California

(Manuscript received 22 September 1993, in final form 15 June 1994)

ABSTRACT

A multiyear simulation with a coupled ocean–atmosphere general circulation model (GCM) is presented. The model consists of the UCLA global atmospheric GCM coupled to the GFDL oceanic GCM; the latter is dynamically active over the tropical Pacific, while climatological time-varying sea surface temperatures (SST) are prescribed elsewhere. The model successfully simulates the main climatological features associated with the seasonal cycle, including the east–west gradient in SST across the equatorial Pacific. The most apparent deficiencies include a systematic cold bias (~2 K) across most of the tropical Pacific and underestimated wind stress magnitudes in the equatorial band. Multichannel singular spectrum analysis is used to describe the multivariate structure of the seasonal cycle at the equator in both the model and observed data. The annual harmonic in equatorial SST is primarily wind driven, while air–sea interaction strongly affects the semiannual harmonic.[1]

1. Introduction

Understanding and predicting El Niño/Southern Oscillation (ENSO) and associated worldwide climate anomalies constitutes a major area of research in seasonal-to-interannual forecasting. Highly simplified coupled ocean–atmosphere dynamical models have shown remarkable success at simulating and even predicting many aspects of ENSO (e.g., Cane et al. 1986; Zebiak and Cane 1987). These simplified anomaly models, however, require the mean climate to be specified, while coupled general circulation models (GCMs) can simulate the complete detailed system. To do so correctly, it is imperative that coupled GCMs capture the mean climate and seasonal cycle. Indeed, ENSO is characterized to a considerable extent by the first oscillatory bifurcation of the climate system from its mean state (Neelin et al. 1994), while the seasonal cycle contributes in an essential way to the timing of warm and cold events (Jin et al. 1994; Tziperman et al. 1994).

One reason why simple anomaly models might succeed at capturing ENSO-like interannual variability is that the latter implies a predominantly adiabatic west–east redistribution of temperature in the ocean mixed layer along the equator, via advection, wave adjustments, and upwelling. The climate-mean and seasonal cycle, on the other hand, are characterized primarily by a large-amplitude, forced oscillation, although advective processes still play an important role, as will become clear through our analyses. Treatment of diabatic processes in GCMs involves parameterizing subgrid-scale processes, which is one of the most difficult components of atmospheric modeling. Thus, realistically simulating the mean climate and seasonal cycle with GCMs may be even more challenging than capturing the physics of ENSO in a model with specified seasonal cycle. The strong interaction between interannual variability and the seasonal cycle means a coupled GCM has to simulate the seasonal cycle in the equatorial Pacific region realistically to predict ENSO. In particular, although coupled GCMs (CGCMs) that exclude the seasonal cycle can exhibit ENSO-like variability (Lau et al. 1992), the precise timing of ENSO events appears to crucially involve the seasonal cycle (Meehl 1990; Jin et al. 1994).

This paper presents detailed analyses of the seasonal cycle of the ocean–atmosphere system in the tropical Pacific, arising in an 11-year simulation with the University of California at Los Angeles (UCLA) coupled ocean–atmosphere GCM. The model consists of a global atmospheric GCM (AGCM) coupled to an oceanic GCM (OGCM) of the Pacific Ocean in the latitudinal band 30°S–50°N. Climatological time-varying land–sea surface conditions are prescribed elsewhere. A brief description of the CGCM is given in section 2. This is followed by a conventional analysis

* Also at Institute of Geophysics and Planetary Physics, University of California at Los Angeles, Los Angeles, CA.

[1] Preliminary results of this research were presented in Mechoso et al. (1991) and Ghil and Mechoso (1992).

Corresponding author address: Dr. Andrew W. Robertson, Department of Atmospheric Sciences, University of California at Los Angeles, 405 Hilgard Avenue, Los Angeles, CA 90095-1565.

of the multiyear mean seasonal cycle in section 3 in terms of composite maps of the tropical Pacific and Hovmoeller diagrams along the equator. Section 4 studies the annual and semiannual harmonics at the equator using multichannel singular spectrum analysis (M-SSA) (Broomhead and King 1986; Vautard and Ghil 1989; Kimoto et al. 1991; Plaut and Vautard 1993). An analogous analysis of observed SST, zonal wind stress, and surface heat flux data is undertaken for comparison. M-SSA is used in Part II of this paper (Robertson et al. 1995) to study the model's interannual variability, and its use in the present paper unifies the treatment of the model's seasonal cycle and interannual variability. The conclusions of Part I follow in section 5.

2. The UCLA coupled GCM

The atmospheric component of the model is a nine-layer, 4° latitude by 5° longitude version of the UCLA AGCM developed by A. Arakawa and collaborators [see Suarez et al. (1983) and references therein]. It is a gridpoint model with a potential-enstrophy-conserving horizontal difference scheme that gives fourth-order-accurate advection of potential vorticity and potential temperature and preserves positive definiteness in water vapor advection. The planetary boundary layer (PBL) is treated as a single well-mixed layer of evolving depth. Bulk assumptions are made for the description of turbulence in the PBL; the surface fluxes of heat and momentum are modeled by Deardorff's (1972) scheme. Both seasonal and diurnal changes are simulated.

When the top of the PBL is above the condensation level, a sublayer of stratocumulus clouds is included that affects radiative fluxes at the surface. Stratus clouds play an important role in the radiation balance over the subsidence regions of the tropical Pacific. Cumulus parameterization is based on the Arakawa and Schubert (1974) scheme, with the effects of vertical redistribution of momentum by convection included. For longwave radiation, the scheme of Harshvardhan et al. (1987) is used. This scheme includes absorption by the water vapor continuum, which plays a crucial role in the Tropics and where the PBL is very humid (Ma et al. 1994). Shortwave radiation is based on Katayama's (1972) scheme, which includes the effects of shortwave absorption by water vapor and CO_2. Cloudiness is interactive, being assumed whenever the predicted relative humidity exceeds saturation or when cumulus convection reaches 500 mb.

The oceanic component is the Geophysical Fluid Dynamics Laboratory model developed by Bryan (1969) and Cox (1984), which has been used and tested extensively for the tropical Pacific by S.G.H. Philander and collaborators (e.g., Philander et al. 1987). The model domain covers the tropical Pacific from 130°E to 70°W and from 28°S to 50°N. The longitudinal resolution is 1°, while in latitude the mesh size is 0.33° between 10°S and 10°N, decreasing gradually poleward to almost 3° at 50°N. The fine mesh near the equator resolves equatorial waves. The model has 27 layers in the vertical, with 10-m resolution in the upper 100 m. The ocean has constant depth of about 4150 m. Vertical mixing by subgrid-scale turbulence is parameterized using the second-order closure scheme of Mellor and Yamada (1982). This formulation was found to give a much better defined thermocline in the eastern Pacific than the Pacanowski and Philander (1981) scheme with its first-order Richardson number dependence (Ma et al. 1994).

The two model components are coupled synchronously: SST is passed to the AGCM and surface fluxes of heat, momentum, and water to the OGCM once per day, averaging out the diurnal cycle. SST outside the OGCM domain is prescribed from an observed monthly climatology. Newtonian cooling is applied at high latitudes in the OGCM to relax temperatures and salinity toward climatology with no smoothing applied at the western boundary. The higher-resolution SST is spatially averaged before being transferred to the AGCM. No "flux correction" is applied to the surface fluxes. The initial state of the 11-year simulation analyzed in this paper corresponds to 15 April of year 9 of a previous simulation with the coupled model that was integrated from an ocean at rest with climatological distributions of mean-monthly temperature and salinity. This previous integration differed only in the details of the treatment of the surface fluxes of heat and moisture at low wind speeds and in including a parameterization of solar radiation penetration into the ocean (see Part II).

3. The mean seasonal cycle

The mean seasonal cycle is defined here in terms of averages for each calendar month over years 2–9 of the simulation. To begin, we inspect maps of the mean simulated fields for March and September over the tropical Pacific and then concentrate on the equator where the seasonal cycle plays a major role in the interannual variability and ENSO (e.g., Meehl 1987). In the Pacific sector, March and September coincide roughly with the extremes of the seasonal cycle, as will be discussed in detail herein.

a. Composite maps of the tropical Pacific

In March, with the sun migrating northward across the equator, both the pattern and magnitudes of simulated SSTs (Fig. 1a) are quite realistic south of the equator (the summer hemisphere), except off the South American coast where values are too warm (cf. Levitus 1982). North of the equator, however, SSTs are too cold across the basin, especially in the west Pacific and off the coast of Mexico (locally up to 5 K). In Septem-

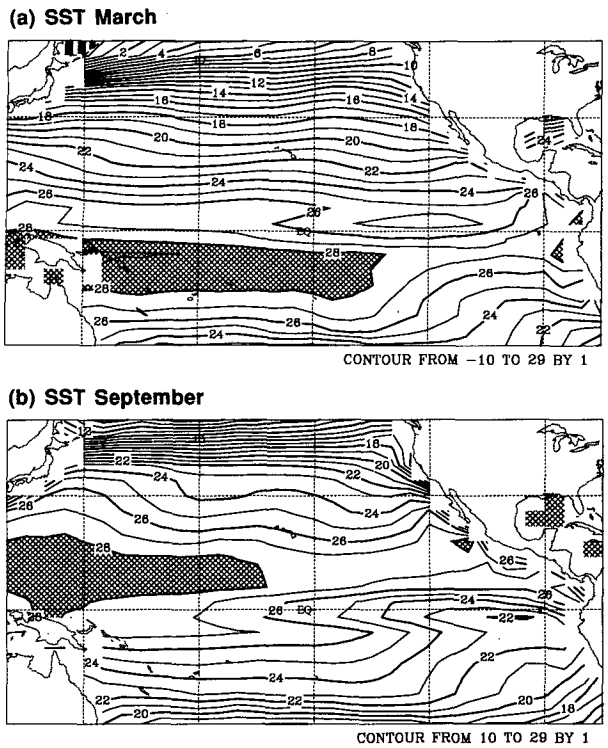

FIG. 1. Maps of simulated mean SST for (a) March and (b) September on AGCM grid. Contours every 1 K, shading above 28°C. These and all other surface maps go from 30°S to 50°N and from 130°E to 70°W; the dotted parallels and meridians are 30° apart and include the equator and date line, respectively.

ber (Fig. 1b), with the sun returning southward, the spatial pattern of simulated SST is quite realistic throughout the central and eastern parts of the basin, although values are too warm off the coasts of California and Peru (locally up to 4 K). In the west Pacific, the warm pool does not extend far enough north or south of the equator, and SST maxima are underestimated by about 2 K. The annual-mean model error in SST is shown in Fig. 3a.

These distributions of SST reflect the accompanying wind stress patterns shown in Fig. 2 to a large extent. Across most of the Pacific equatorial band, both the SST and wind-stress patterns tend to vary in phase, implying that the SST is in approximate equilibrium with the seasonally varying wind-stress forcing. Figures 1 and 2 indicate that large (small) wind stresses tend to be associated with cold (warm) SSTs, possibly involving an "evaporation feedback" off the equator (see below) and an upwelling on the equator. Integrated over the basin, however, this is not the case: model SSTs are underestimated despite the weak surface winds (Fig. 3).

The general pattern of amplification and meridional extension of the winter trade winds and their associated wind stress are realistic when compared with the pseudostress-observed climatology of Stricherz et al. (1992). The northeast trades in March, however, are displaced—or extend—too far south in the eastern Pacific, with the intertropical convergence zone (ITCZ) displaced south of the equator. In addition, the northeast trades are too strong west of the date line. The southward shift of the northeast trades in March is associated with colder than observed SSTs north of the equator at this time, although the corresponding Ekman transport is poleward. These cold SSTs are consistent with large surface fluxes of latent heat near 10°N (Fig. 4a). Advection of relatively dry, cooler air from the subtropics is in turn consistent with a local increase in evaporation and a cooling of the ocean surface. Once SSTs fall by this process, deep convection may be suppressed, effectively displacing the ITCZ southward. This is also consistent with a further drying of the PBL north of the equator as a consequence of entrainment of air from the free atmosphere, thereby enhancing the process. The parameterizations in the AGCM component of our coupled model (e.g., the PBL and deep convection) may be especially sensitive to this chain of events. In this way, air–sea interaction processes in the coupled GCM might be responsible for the simulated ITCZ being displaced southward of its observed position in northern winter via an evaporative-feedback mechanism. South of the equator, the simulated southeast trades and their associated stress tend to be realistically strong east of 120°W but fail to extend far

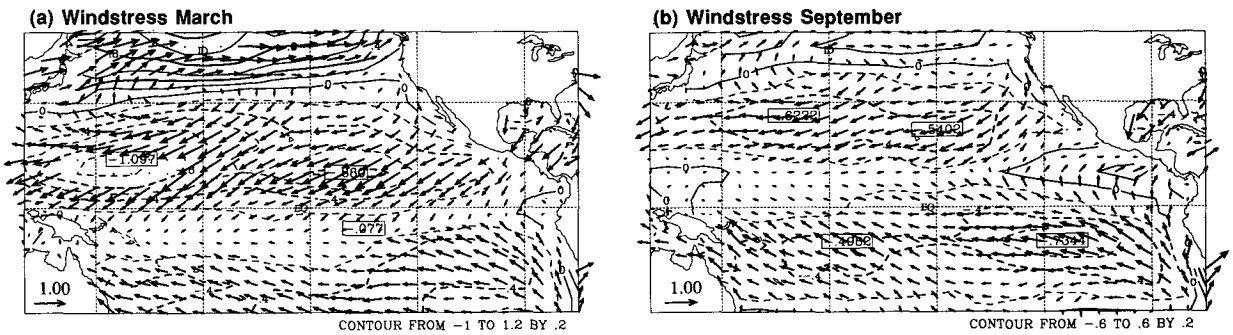

FIG. 2. Simulated wind stress in dyn cm^{-2}; as in Fig. 1. Contours are of the zonal component. Maximum vector is 1.0 dyn cm^{-2}.

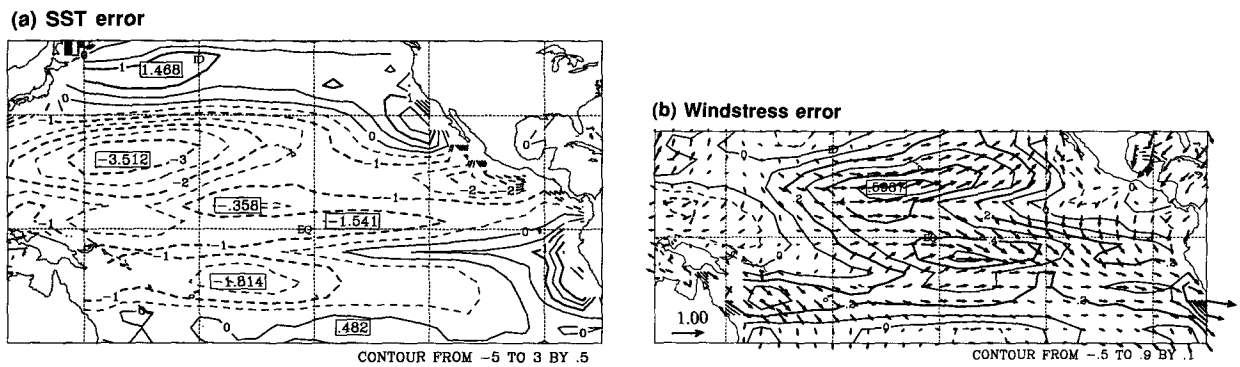

FIG. 3. Annual mean model error. (a) SST (°C): CGCM minus Levitus (1982) observed climatology, (b) wind stress (dyn cm^{-2}): CGCM minus the FSU pseudostress climatology 1982–1991 (Stricherz et al. 1992) with $C_D = 1.5 \times 10^{-3}$.

enough westward. Their domain of influence is confined south of the equator in March. The strong southeast trades near the date line in September are associated with much weaker latent heat fluxes than those north of the equator in March (Fig. 4b), indicative of little evaporation feedback here.

The annual-mean difference between the simulated wind stress and that estimated from surface-wind observations by Stricherz et al. (1992) is shown in Fig. 3b. Simulated wind stress magnitudes are underestimated in the equatorial belt on average, especially in the zonal component over the central Pacific and in the meridional component over the eastern Pacific. An uncoupled integration with the AGCM using observed SSTs also underestimates the equatorial wind stress magnitudes. This deficiency may be associated with a lack of momentum mixing by shallow clouds (A. Arakawa 1993, personal communication). In our model, however, the strength of the equatorial easterlies scarcely increases above the PBL. Further preliminary experiments (J. D. Farrara 1993, personal communication) suggest that introducing a simple vertical mix-

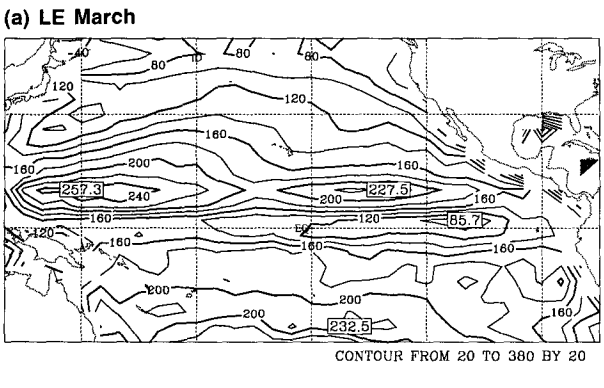

FIG. 4. Simulated latent heat flux at the sea surface in W m^{-2}; as in Fig. 1.

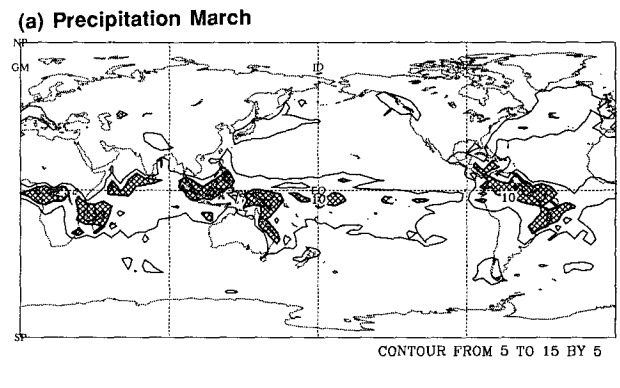

FIG. 5. Simulated global precipitation in mm day^{-1}; as in Fig. 1. Values > 10 mm day^{-1} are hatched.

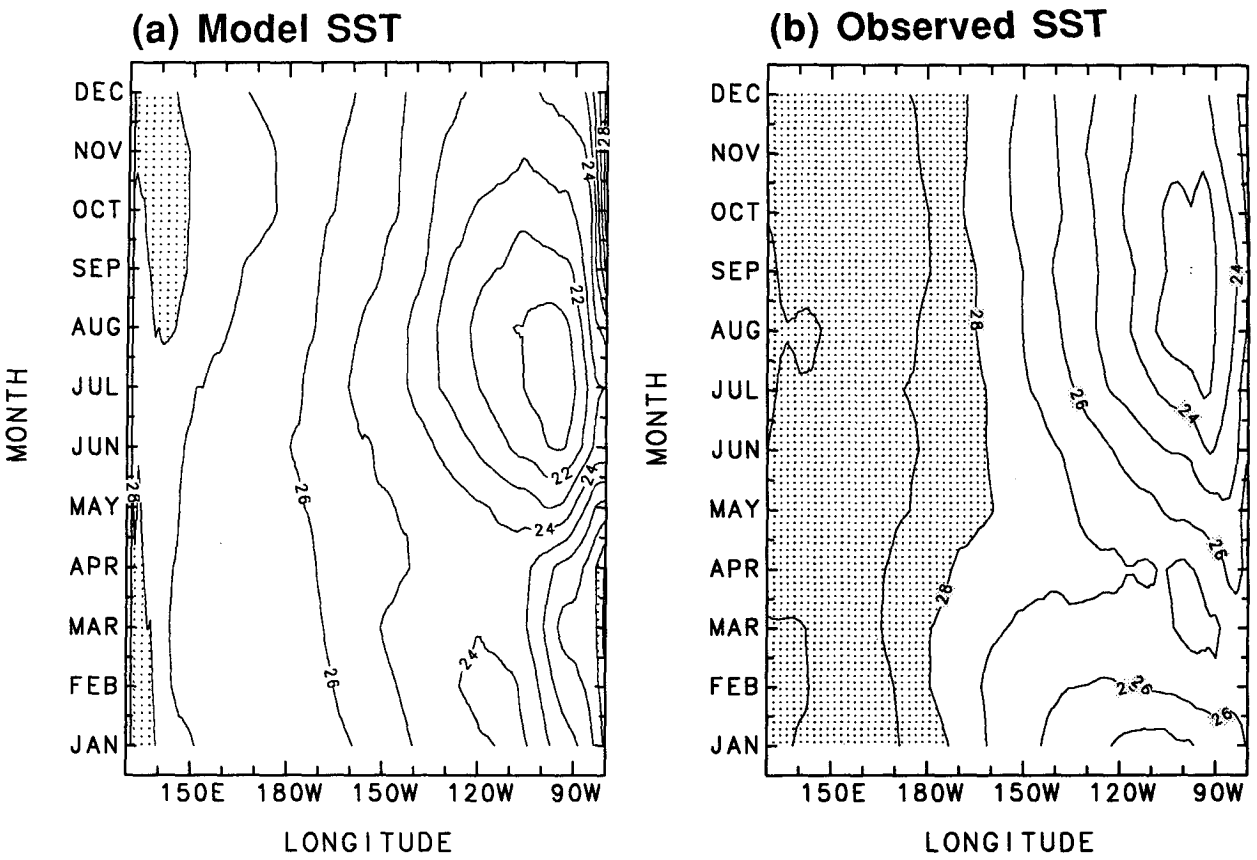

FIG. 6. The mean seasonal cycle of SST at the equator. (a) CGCM (on OGCM grid) and (b) observed (NMC Climate Analysis Center blended analysis for 1982–1991; Reynolds 1988). Contour interval is 1 K, stippling is >28°C.

ing of momentum would not alleviate the problem. Note that outside the equatorial belt the error in Fig. 3b is relatively small and the surface winds are quite reasonably simulated.

Along the coast of South America, SSTs are too warm throughout the year (Fig. 3a), suggestive of underestimated coastal upwelling and probable underestimation of the PBL stratus albedo. Concerning the upwelling, Fig. 3b shows anomalous *onshore* surface winds, perhaps associated with failure to correctly represent the effects of the Andes on the atmospheric circulation, given the relatively smooth topography of the AGCM. Indeed, the uncoupled integration of the AGCM mentioned in the previous paragraph indicates similar features. The apparent lack of coastal upwelling is consistent with an underestimated northward geostrophic transport of cold water by the Peru current; that in turn agrees with overestimated SSTs on the southern flank of the cold tongue in September, making it a narrow upwelling phenomenon. This might tend to reduce sea level pressure over the region, allowing the northeast trades (with the ITCZ) to penetrate south of the equator (Philander et al. 1992). Overestimated SSTs off the coasts of Peru and California are a common problem in current coupled GCMs, and our model performs comparatively well. Stratus clouds are present in the UCLA CGCM, which may contribute to smaller errors compared to other coupled GCMs that do not include their effects.

Figure 5 shows the global precipitation patterns for March and September. Over the tropical Pacific the precipitation maxima demarcate the zones of deep convection and large-scale low-level convergence that tend to coincide with the warmest waters. Consistent with Figs. 1 and 2, there is an ITCZ in September with a South Pacific convergence zone (SPCZ) in March. The rainfall maxima migrate with the season following the warmest water across the equator. However, both the SPCZ and the ITCZ are too weak—consistent with underestimated SST—and the ITCZ is displaced south of the equator in March. There is a tendency toward a double ITCZ straddling the equator, a feature consistent with the above-mentioned "equatorial doldrums."

b. Hovmoeller diagrams along the equator

We now focus on the time evolution of the seasonal cycle at the equator. Figure 6 presents Hovmoeller dia-

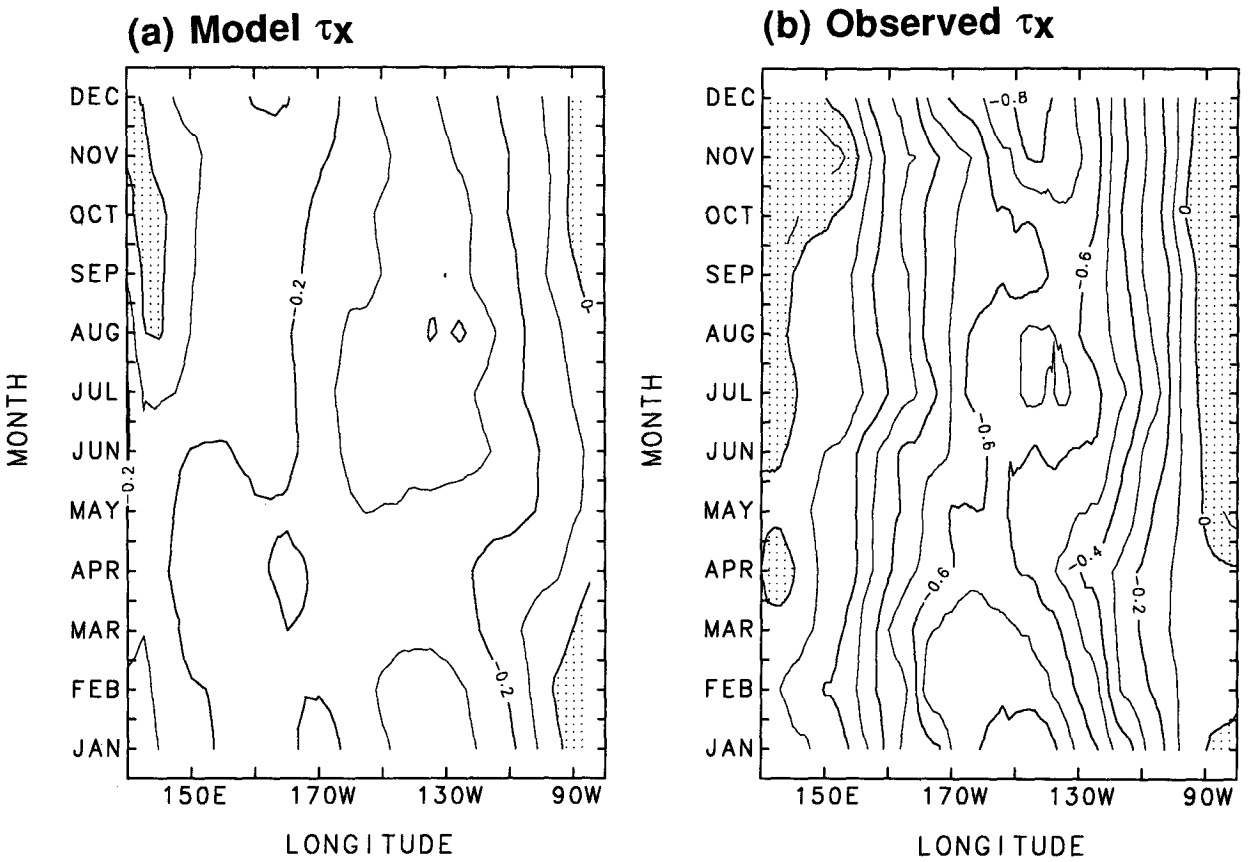

FIG. 7. The mean seasonal cycle of equatorial zonal wind stress (4°S–4°N). (a) CGCM and (b) observed (FSU, as in Fig. 3). Contour interval is 0.1 dyn cm^{-2}; positive values are stippled.

grams of simulated and observed monthly mean SST along the equator. The simulated values are systematically about 2 K too cold at the equator. The pronounced seasonality of the cold tongue in the east Pacific is simulated, although it develops about two months prematurely and is slightly too strong. At its maximum in July, the SST difference across the basin is comparable with that observed, and zonal gradients on the equator are realistic. However, the model's cold tongue is very narrow, so that on the AGCM grid—averaging SST from 4°N to 4°S—the zonal gradient is underestimated in the central basin, and the cold tongue is less pronounced (not shown). In northern spring, SSTs remain too cold around 120°W (compare Fig. 1a), associated with the overestimated southward extension of the northeast trades.

The corresponding figures of equatorial zonal wind stress are shown in Fig. 7. A simulated maximum of 0.4 dyn cm^{-2} is reached in August near 130°W, with a weak secondary maximum in December. The simulated maxima are about one-half the magnitude of the inferred observed maxima but extend over a broader longitudinal band, consistent with the underestimated zonal gradient in SST in the central Pacific, averaged from 4°N to 4°S. Since the model's SST gradient at the equator itself is reasonable, the mismatch in grid size between the two component models may be of consequence. The timing and longitude of the simulated maxima compare well with the observed climatology, but both the mean and standard deviation are underestimated in the central Pacific.

Figure 8 shows the seasonal cycle along the equator in rainfall and evaporation (in terms of the latent heat flux). Simulated rainfall and evaporation over the equatorial Pacific follow SST to a first approximation, both in zonal distribution and seasonal variation. In particular, the cold tongue is associated with relatively low evaporation and rainfall. Thus, evaporation and cloudiness associated with precipitation generally produce negative feedbacks on SST anomalies with respect to the annual mean. Rainfall compares well with Oberhuber's (1988) estimates, while the model overestimates evaporation west of the date line and in the eastern Pacific in northern spring.

The net heat flux into the equatorial Pacific is shown in Fig. 9 for both the model and the observed climatology of Oberhuber (1988). West of the date line, the simulated net surface flux is realistically small, asso-

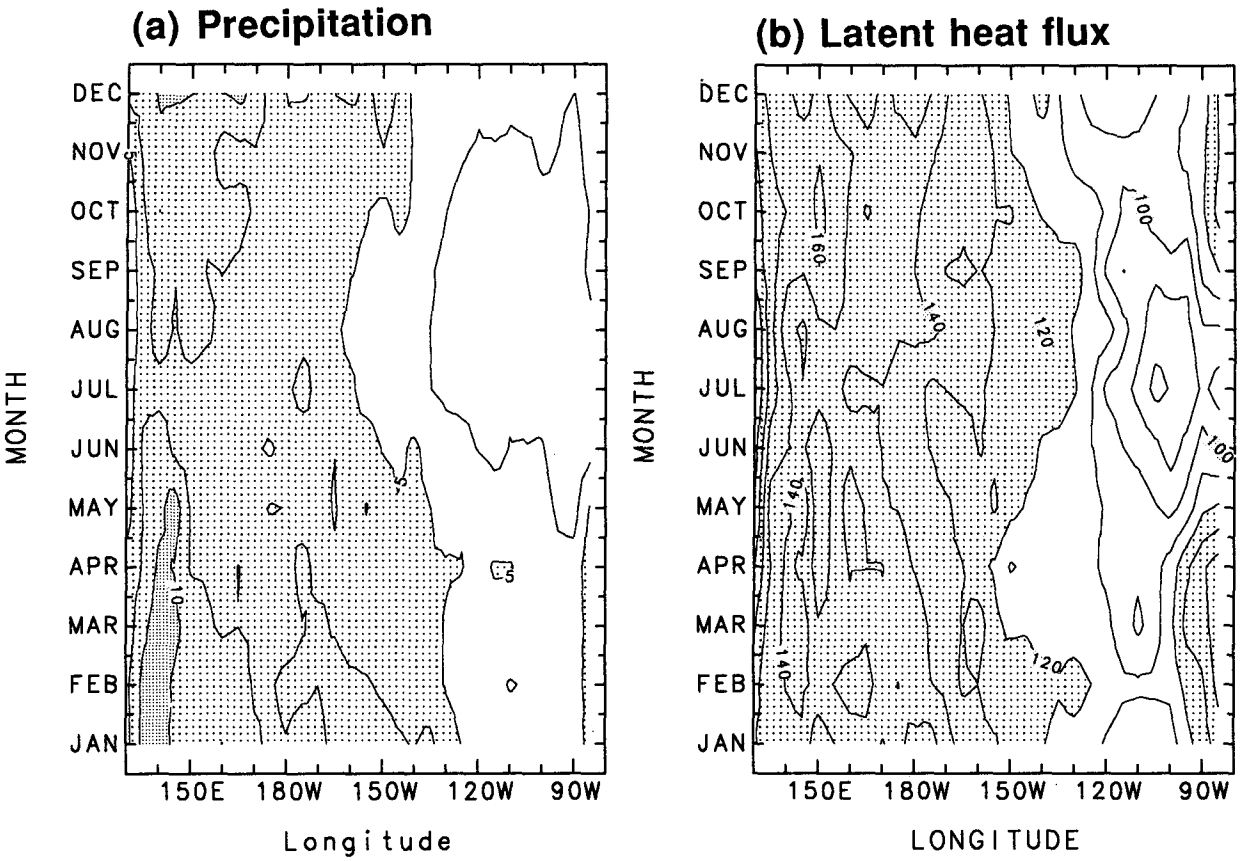

FIG. 8. Simulated mean seasonal cycle of equatorial (4°S–4°N) (a) precipitation (2.5 mm day^{-1}, light stippling: 5–10 mm day^{-1}), (b) latent heat flux (10 W m^{-2}, stippling >120 W m^{-2}).

ciated with strong evaporation and attenuation of the shortwave flux by the cloud cover accompanying precipitation. The net flux into the model's ocean is realistically large in the eastern Pacific in March but its semiannual variation is too large. We shall examine this in greater detail at the end of section 4.

c. *Cross sections through the ocean*

Zonal cross sections of simulated ocean temperature and zonal current along the equator appear in Fig. 10, again for March and September. Enhanced vertical temperature gradients associated with the thermocline are present, though rather diffuse. The core of the undercurrent coincides with the thermocline. Its intensity increases from a minimum in January (~40 cm s^{-1}) to its maximum near 150°W in June (~70 cm s^{-1}). Both the maximum and the seasonal variation are underestimated, consistent with the rather flat thermocline in the central Pacific and the underestimated equatorial wind stress. The phase is somewhat retarded: there is less of a springtime "surge" of the undercurrent seen in OGCM studies (Philander et al. 1987). This agrees with the lack of a marked spring minimum in equatorial zonal wind stress (Fig. 7a), traceable to the anomalous southward extension of the northeast trades (Fig. 2a). The longitudinal position of the undercurrent maximum shifts eastward between March and September, as does the thermocline's maximum east–west slope, although inertial effects are probably also important (Philander and Chao 1991). The undercurrent does not outcrop at the surface during northern spring, which is consistent with the persistence of cold SSTs around 120°W throughout the year (Fig. 6) and the exaggerated southward shift of the northeast trades in northern spring. The climatological isotachs indicate the existence of short waves in September but not March. This phenomenon has been noted by Philander (1978) and interpreted in terms of the presence of a 30-day instability in September when the latitudinal shear of the currents is strong.

Meridional sections for both months at 135°W are shown in Fig. 11. The north equatorial countercurrent outcrops at the surface between July and December, in agreement with the uncoupled OGCM results of Philander et al. (1987), and peaks in November–December (20 cm s^{-1}), disappearing in May–June. The

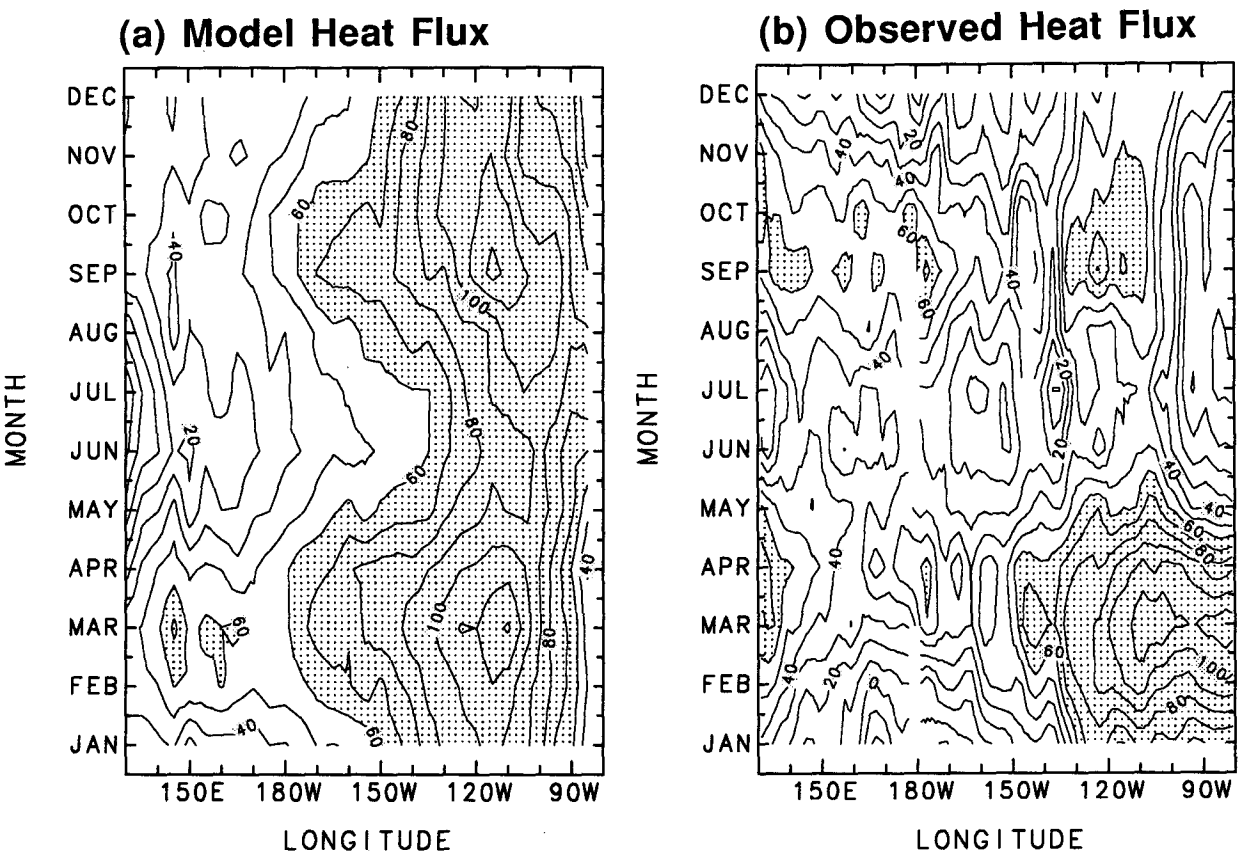

FIG. 9. Net heat flux into the ocean (a) model (4°S–4°N) and (b) observed climatology of Oberhuber (1988) (3°S–3°N). Contour interval is 10 W m^{-2}, with stippling >60 W m^{-2}.

maximum current intensity is again underestimated. Associated with the countercurrent, the thermal field in September exhibits a ridge near 10°N and a trough near 3°N. The seasonal cycle of the south equatorial current is reproduced, although the current intensity is underestimated once more, especially close to the surface. Consistent with the underestimated zonal currents, the Ekman drift velocities and the upwelling, which reaches a maximum of 250×10^{-5} cm s^{-1}, are also underestimated. The model captures the downwelling in September associated with convergent meridional flow in the surface layers in the region of the countercurrent.

To summarize, the simulated seasonal cycle in the tropical Pacific is in general encouragingly realistic. All the ocean currents in the equatorial zone are captured, although they are systematically too weak, because of the underestimated wind stress magnitudes. The northeast trades are displaced too far south in northern winter, and this may be connected with the premature development of the cold tongue. These deficiencies may involve air–sea interaction processes, including evaporation feedback. A lack of coastal upwelling and associated weakness of the Peru current may result in overestimated SST and underestimated sea level pressure over the Peru current region, allowing the northeast trades to extend farther southward. Deficiencies in the simulation of PBL stratus may also contribute to this feature.

4. The annual and semiannual cycles at the equator

Singular spectrum analysis (SSA) decomposes a time series into a set of oscillatory and nonoscillatory components by expanding in terms of an optimal orthonormal basis, whose leading mode corresponds to the leading axis of the ellipsoid of states in the model's phase space. Using SSA to investigate the seasonal cycle at the equator is attractive for several reasons: 1) It easily identifies the annual and semiannual cycles, although they may not be purely sinusoidal. 2) It situates the seasonal cycle in the context of the model's climatic variability as a whole, providing a unified picture with the lower-frequency modes that are the subject of part II. 3) It yields a direct description of the seasonal timescale structure of the CGCM's climatic attractor (Ghil et al. 1991), without having to make recourse to month-by-month averages.

a. Singular spectrum analysis

M-SSA is an extension of the principal component analysis of a time series of spatial vectors (i.e., an anal-

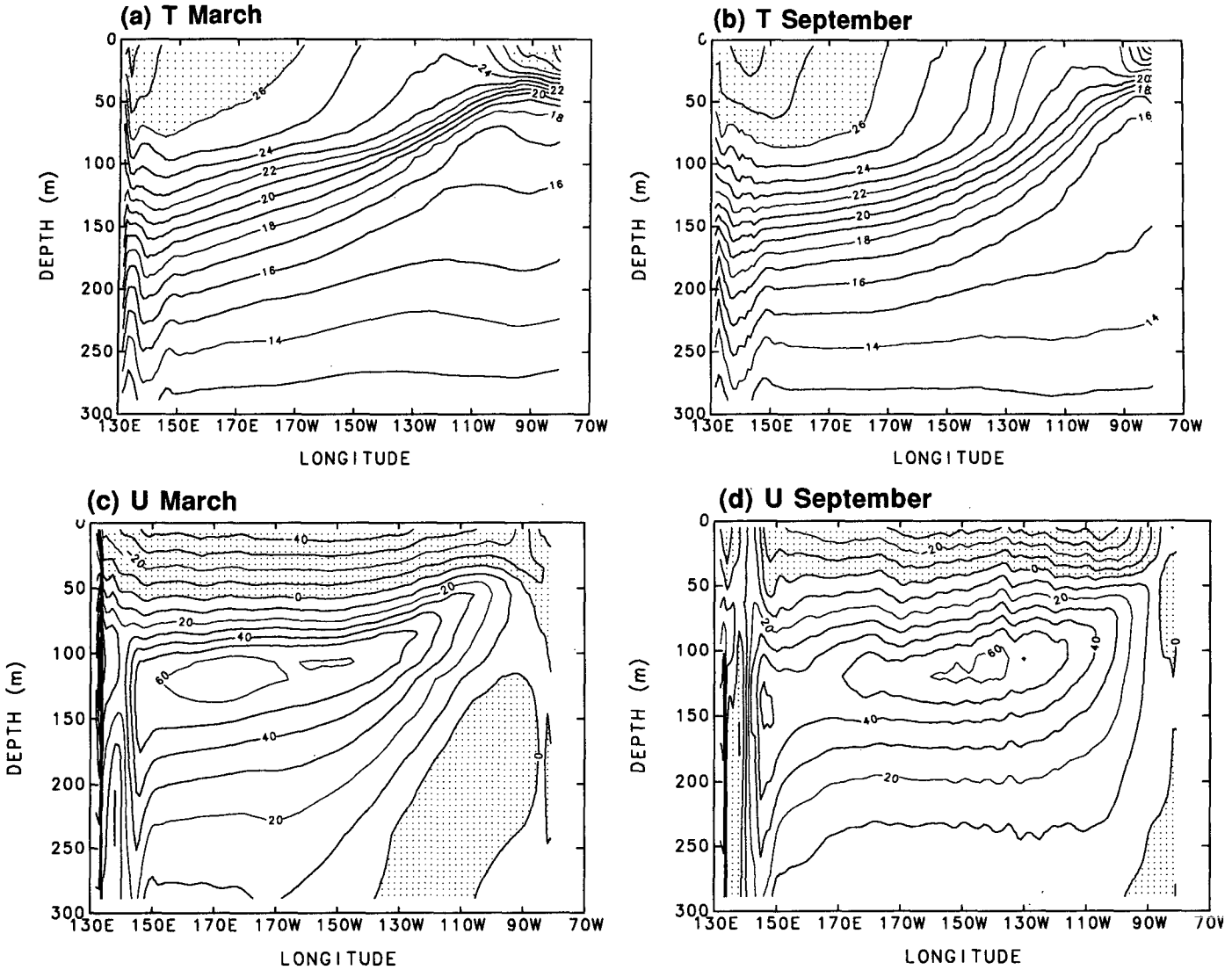

FIG. 10. Equatorial depth–longitude cross sections of model ocean temperature for (a) March and (b) September (contour interval is 1 K; values above 26°C are stippled), and model zonal current velocity for (c) March and (d) September (contour interval is 20 cm s^{-1}; negative values are stippled).

ysis of covariance) to include additionally an analysis of temporal structure (i.e., autocovariance). It is based on a sequence of state vectors, each consisting of M-lagged copies of a spatial vector (including lag zero). At time i, the state vector can be written $x_i = (x_{1,i}, x_{1,i+1}, \cdots, x_{1,i+M-1}, x_{2,i}, x_{2,i+1}, \cdots, x_{2,i+M-1}, \cdots, x_{L,i}, x_{L,i+1}, \cdots, x_{L,i+M-1})^T$, where the first subscript refers to the spatial grid point or "channel," of which there are L in number. The complete sequence of state vectors $\mathbf{x}_i$ defines the *trajectory matrix* $\mathbf{X}$, which contains a complete record of the $N - M + 1$ (space-time) patterns that have occurred within the "window" defined by the maximum lag; namely, $\mathbf{X} = (\mathbf{x}_1^T, \mathbf{x}_2^T, \cdots, \mathbf{x}_{N-M+1}^T)^T$, where N is the length of the time series (Broomhead and King 1986). By the Karhunen–Loève theorem, the eigenmodes $\mathbf{e}^k$, $1 \leq k \leq L \times M$ of the covariance matrix $\mathbf{X}^T\mathbf{X}$ optimally partition auto and cross covariances in the data into orthonormal modes according to the variance they account for (which is given by the respective eigenvalue). A singular-value decomposition of $\mathbf{X}$ is in practice an efficient method of obtaining these modes for the short time series considered here. The eigenmodes of $\mathbf{X}^T\mathbf{X}$ correspond to the right-singular vectors of $\mathbf{X}$, whose singular values are the square roots of the corresponding eigenvalues and give SSA its name. Vautard and Ghil (1989) recognized that pairs of nearly equal eigenvalues correspond to oscillatory modes. The data may thus be expanded into a set of oscillatory and nonoscillatory modes,

$$x_{l,i+j} = \sum_{k=1}^{L\times M} a_i^k e_{l,j}^k, \quad 1 \leq l \leq L, \quad 0 \leq j \leq M-1, \tag{1}$$

where the projection coefficients a_i^k are the principal components (PCs). This "method of delays" (Broomhead and King 1986) is algorithmically equivalent to extended Empirical Orthogonal Function (EOF) analysis (Weare and Nasstrom 1982), but with greater emphasis on the temporal structure of the variability.

In the case of the seasonal cycle, the periods of the constituent harmonics are known a priori so that a Fourier transform could be used. SSA, however, overcomes the quandary of the higher harmonics, defining in some sense precisely what is meant by the "seasonal cycle" in terms of an annual and semiannual cycle. The SSA basis functions (i.e., the temporal EOFs) are empirical and are thus not constrained to be sines and cosines, as in the case of harmonic analysis. In practice, however, the annual and semiannual cycles resulting from SSA approach sine waves—i.e., the annual and semiannual harmonics. SSA also enables the seasonal cycle to be directly compared with the lower-frequency ENSO modes, which are the subject of Part II of this paper. It further provides an indication of the signal-to-noise ratio associated with the annual and semiannual cycles.

b. *The annual and semiannual cycles*

We now apply M-SSA to model fields of equatorial SST, zonal wind stress, thermocline depth, and also to ocean currents and surface heat fluxes. The analysis is carried out for each variable separately, using 4°N–4°S averages every 5° of longitude (the AGCM grid) for atmospheric quantities and SST, and 2° longitudinal averages at the equator for oceanic quantities. The longitudinal domain considered is 140°E–85°W. The 11-year time series for each channel (i.e., grid box) was first centered (i.e., the time mean subtracted) and normalized by its standard deviation so that the elements of $\mathbf{X}^T\mathbf{X}$ are correlations. A window size of 12 months ($M = 13$) is used, which is suitable for resolving periods of 3–12 months (Vautard et al. 1992).

The results are summarized in Table 1 in terms of the modal pairs (of nearly equal eigenvalues) representing the annual and semiannual cycles. These modal pairs were identified from the eigenvalue spectrum—with that of the annual cycle being well separated from the rest of the spectrum in most cases—and by inspecting the associated PCs, which are almost purely sinusoidal. The associated modal structures are given by the respective eigenvectors, though these have arbitrary phase and amplitude. To facilitate comparison with the mean seasonal cycles in Figs. 6 and 7, we reconstruct the original time series using the appropriate modal pair and form multiyear means for each month. From (1) there are as many ways of doing this as there are lags, but averaging over all possible reconstructions via (1) is optimal in a least-squares sense (Vautard et al. 1992).

These "reconstructed components" (RCs) of the annual cycles of simulated SST, zonal wind stress (τ_x), and thermocline depth are illustrated in Fig. 12 over two cycles. The modes have much more amenable structures than monthly mean anomaly maps (not shown). Figure 12 highlights the temporal phase lag of SST behind τ_x at the eastern boundary by about three months (i.e., one-quarter period), suggestive of periodic forcing by the wind. It also highlights the marked westward propagation in the annual cycle of τ_x in the east Pacific. This contrasts with the SST pattern, which exhibits only a slight, but perceptible, westward propagation. Thus, as the τ_x anomaly propagates rapidly westward away from the coast, SST and τ_x anomalies become temporally in phase later in the cycle, with the τ_x anomaly displaced to the west of the SST one. Coupling between the surface layer of the ocean and the atmosphere is known to favor this spatial configuration (Neelin 1991).

Table 2 and Fig. 13 present the results of similar analyses for observed SST and zonal wind stress data (see caption of Table 2). In this case, a window length of 5 years ($M = 61$ months) was used, since the observed time series contained substantial interannual variability, which a 12-month window had trouble separating from the annual cycle. The annual and semiannual cycles account for a much smaller portion of the total observed variance (about half) than of the CGCM variance (Table 1). This is simply because there is more interannual variability in the observed fields and is not the result of using different window lengths.

The annual cycle of observed SST (Fig. 13) is remarkably similar to that of the CGCM in the eastern Pacific in both phase and amplitude. However, the model does underestimate its westward propagation, and the model's annual cycle leads the observed one by about one month. Notably, the annual cycle of the simulated zonal wind stress at the equator is only about half as strong as that inferred from the Florida State University (FSU) pseudostress product, although its rate of westward phase propagation in the eastern Pacific is realistic. The model's temporal phase error in τ_x in the eastern Pacific is similar to that of SST (about one month), and simulated anomalies of τ_x are displaced too far eastward. West of 150°W, the annual cycle of zonal wind stress is poorly simulated. Nevertheless, these wind errors in the western Pacific seem to be of little consequence to the annual cycle in SST, which is concentrated in the east Pacific.

Even in the annual cycle of the observed fields, the rate of westward propagation of τ_x exceeds that of SST. Zonal asymmetries in the trade winds associated with continental asymmetries may account for the westward displacement of zonal wind-stress anomalies along the equator, so that the meridional displacement of the

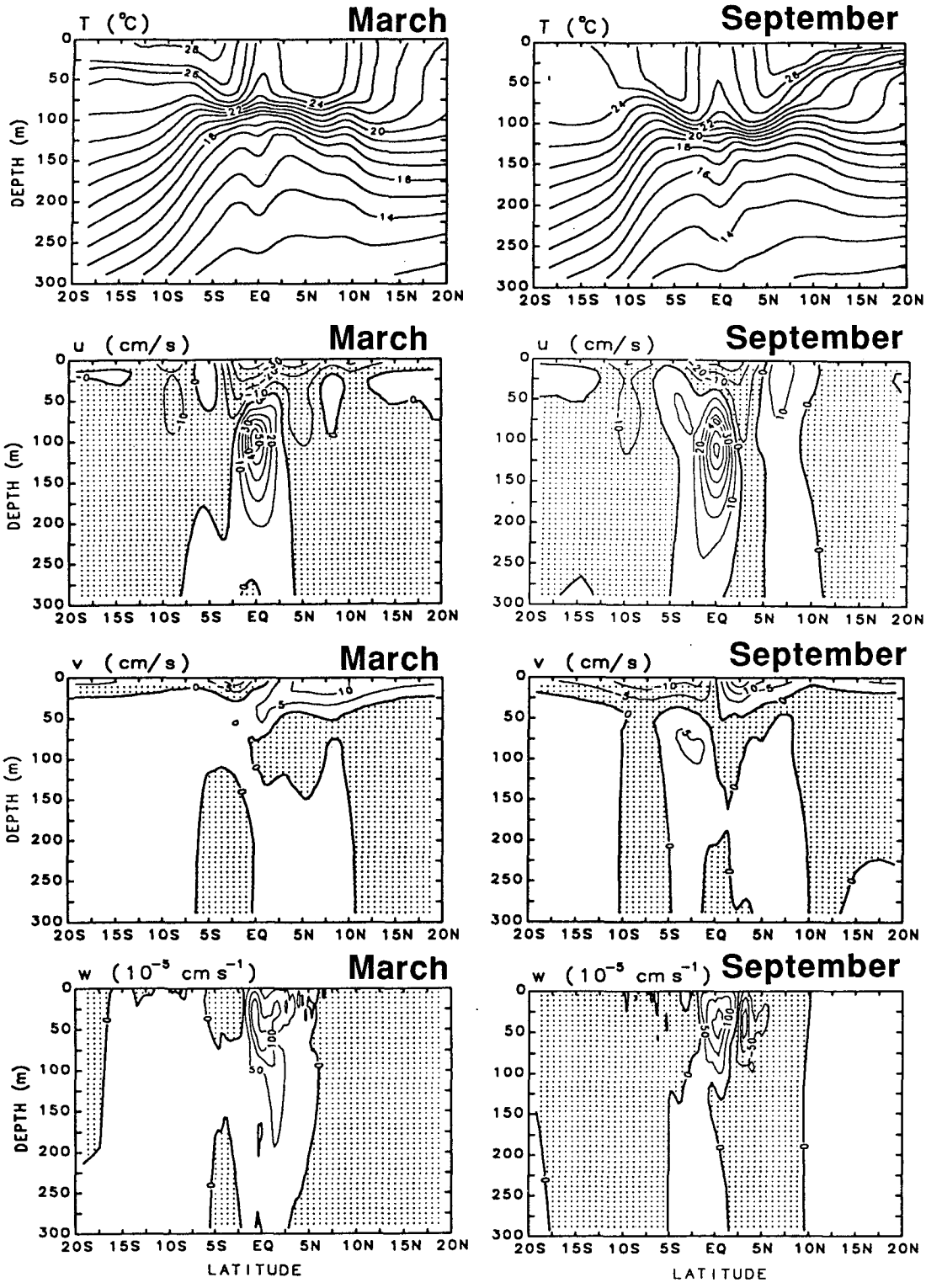

FIG. 11. Meridional ocean cross sections of model temperature and current velocities at 135°W from 20°S to 20°N for March and September.

TABLE 1. The M-SSA of the CGCM seasonal cycle in the equatorial Pacific. Tabulated is the modal pair (e.g., 1–2) that represents the annual and semiannual cycles, with the percentage of associated variance below it. The thermocline depth is taken as the depth of the 20°C isotherm. The equatorial undercurrent is the zonal current velocity averaged over 100–150-m depth, with the equatorial surface current averaged 0–30 m. The equatorial upwelling is averaged over 25–95-m depth. A dash indicates that no modal pair was identified among the leading reconstructed components (RCs).

Model field	Annual cycle	Semiannual cycle
SST	1–2	5–6
	50.9	10.3
τ_x	1–2	3–4
	31.8	8.2
Thermocline depth	1–2	5–6
	63.1	4.8
Surface current	1–2	—
	43.0	
Undercurrent	1–2	—
	59.0	
Upwelling	1–2	—
	22.4	
Sea level pressure	3–4	1–2
	23.1	28.4
Net heat flux	3–4	1–2
	20.0	35.1
Latent heat flux	1–2	3–4
	14.0	6.6

trade wind belts with the seasons could give rise to an apparent zonal propagation of anomalies along the equator. On the other hand, it has been suggested that the westward propagation of anomalies associated with the seasonal cycle might arise from air–sea interaction involving the seasonal cycle of convection and surface wind convergence and from advection by the frictional currents in the oceanic mixed layer (Horel 1982; Meehl 1990; Neelin 1991). A ratio of the magnitudes of stress to SST anomalies associated with the annual cycle can be inferred from Figs. 12 and 13 to be about 0.025 and 0.05 dyn cm^{-2} K^{-1} for the model and observed data, respectively.

The annual cycle of the model's thermocline depth (Fig. 12c) has a distinctive uniform eastward propagating structure (phase speed ~ 1 m s^{-1}) that peaks toward the east of the basin. There is evidence of Sverdrup balance, and thermocline anomalies (of the opposite sign) lead those in SST near the eastern boundary by one to two months. This type of structure has also been found in a linear shallow-water model subject to a periodic, zonally uniform wind stress forcing of broad meridional extent (Cane and Sarachik 1981). Observations of thermocline depth at the equator (Meyers 1979) indicate that the observed annual harmonic of the depth of the 14°C isotherm peaks at the eastern boundary, with a secondary peak near 150°W. The CGCM is in good agreement with this. However, the phase propagation of Meyers' (1979) annual harmonic is small west of 130°W (and even westward west of the date line) and only about 20 cm s^{-1} eastward east of 130°W. The ratio of anomaly magnitudes of thermocline depth to SST for the model's annual cycle is about 7 m K^{-1}.

Figure 14 shows the ocean current structure of the annual cycle. The zonal equatorial currents delineate two longitudinal domains. East of 120°W, the zonal currents and upwelling exhibit westward propagation, with the surface current and upwelling being in phase with τ_x (Fig. 12b) and the undercurrent (Fig. 14b) being almost in quadrature with the surface current (Fig. 14a). Thus, the surface current and the upwelling (Fig. 14c) appear to be in equilibrium with the local wind, while the undercurrent appears to be primarily a local response to periodic forcing by the local wind so that it is in quadrature with it. West of 120°W, the surface current anomaly structure is—to a first approximation—a smoothed version of τ_x, with the undercurrent again in approximate quadrature with it. The eastward shift of the undercurrent maximum with the season agrees with Fig. 10, although the amplitude is smaller in Fig. 14b where the undercurrent anomalies are averaged from 100 to 150-m depth. Upwelling anomalies tend to be in phase with those of thermocline depth west of 120°W.

Figure 15 illustrates the semiannual cycle over two periods, that is, 1 year (note the different ordinate and the smaller contour intervals compared to Fig. 12). This mode differs significantly from the annual cycle or the interannual modes of Part II. Near the eastern boundary, the signatures of SST and τ_x propagate westward in tandem, and sea level pressure anomalies (not shown) are in antiphase with those of SST. Furthermore, anomalies of τ_x are situated just west of those of SST. Both are very suggestive of air–sea interaction involving advection by frictional currents in the ocean mixed layer (Neelin 1991). Equally striking is the standing oscillation in thermocline depth—quite unlike the eastward propagating structures that characterize the annual cycle, or the low-frequency modes of Part II. This thermocline structure reflects Sverdrup balance with a localized anomaly in τ_x. Contrasting with the model, the observations of Meyers (1979) suggest that the semiannual harmonic of thermocline depth peaks at the eastern boundary.

Figure 16 shows the semiannual cycles of equatorial SST and zonal wind stress from our observed datasets. The SST (Fig. 16a) is quite well simulated by the model in phase, amplitude, and westward propagation. The simulated maxima are, however, unrealistically confined to the eastern boundary. As in the annual cycle, the phase of the zonal wind stress mode is reasonable from 120° to 150°W, but amplitudes are only about half of those observed. Interestingly, east of 120°W, the observed mode is weak, as noted by Meyers (1979), and does not agree with the westward propagating structure seen in the simulated

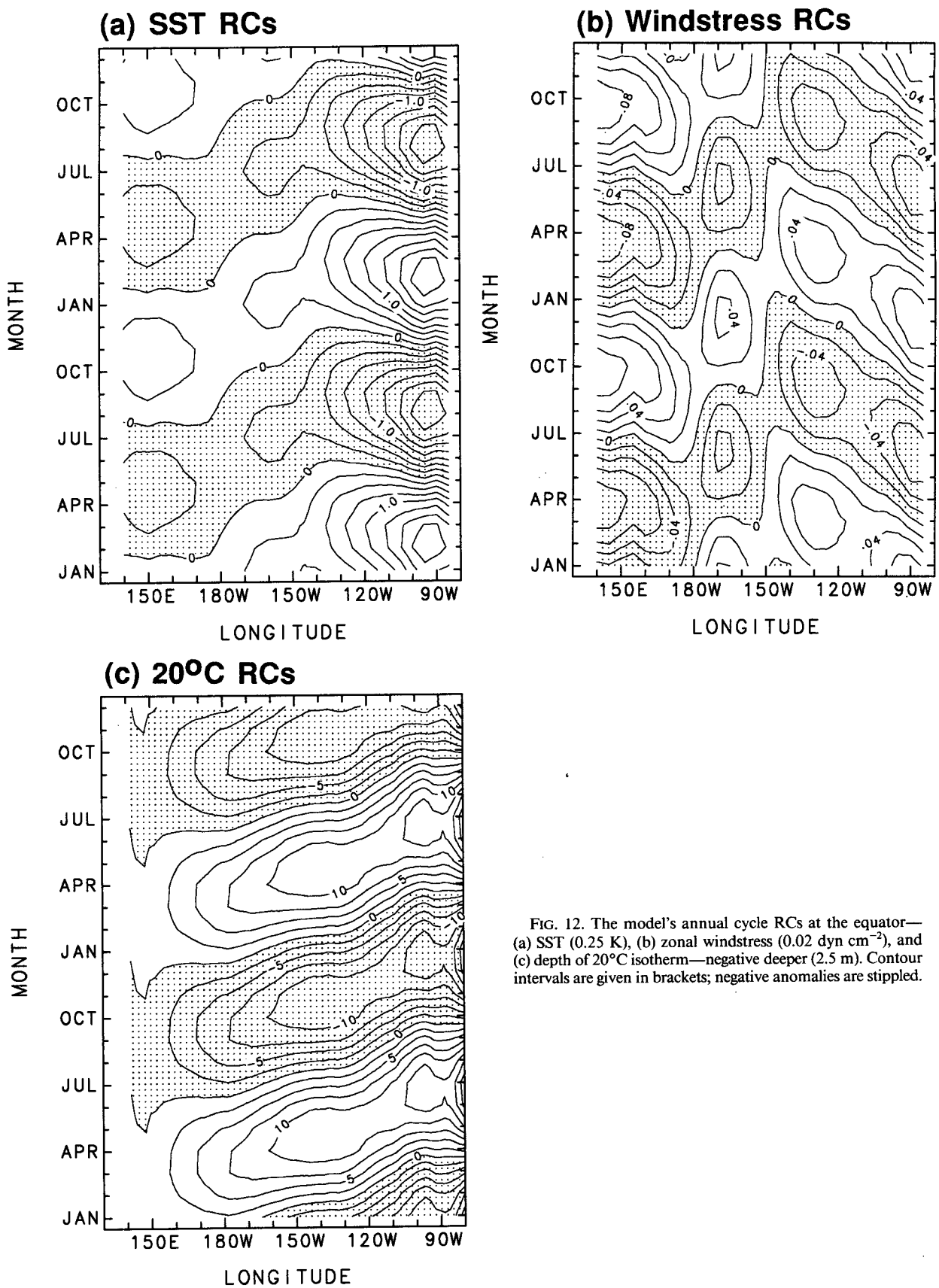

FIG. 12. The model's annual cycle RCs at the equator—(a) SST (0.25 K), (b) zonal windstress (0.02 dyn cm^{-2}), and (c) depth of 20°C isotherm—negative deeper (2.5 m). Contour intervals are given in brackets; negative anomalies are stippled.

TABLE 2. The M-SSA of the observed seasonal cycle in the equatorial Pacific. Same as Table 1 except using a window length of 5 years. SST analysis: NMC data (as in Fig. 6), averaged over 3°S–3°N; τ_x analysis: FSU data (as in Fig. 3), averaged over 4°S–4°N; both with 35 4° longitude-average channels 140°E–80°W.

Observed field	Annual cycle	Semiannual cycle
SST	3–4	7–8
	23.2	5.1
τ_x	3–4	7–8
	15.6	6.2

semiannual cycle of τ_x. West of 150°W, the semiannual cycle in simulated zonal wind stress is weaker than observed. The model's semiannual cycle has a stress-to-SST ratio of about 0.07 dyn cm^{-2} K^{-1}, versus 0.2 dyn cm^{-2} K^{-1} in the observations. These values are larger than those of the annual cycle and closer to those of the low-frequency modes (Part II), especially for the observed data. This is consistent with the structural evidence that the semiannual mode is more a product of air–sea coupling than the annual mode. No semiannual mode could be isolated in the zonal equatorial currents, indicating that their semiannual variation is weak.

Figures 17 and 18 show, respectively, the annual and semiannual cycles of the net heat flux into the ocean at the equator. Each figure contrasts the CGCM simulation with the observed monthly climatology of Oberhuber (1988). The M-SSA of the latter is based on 8° × 8° latitude–longitude averages centered on the equator; we use a 12-month window, with the 12-month climatology repeated four times. In the eastern Pacific, shortwave radiation anomalies dominate the model's annual cycle west of 110°W, with latent heat flux anomalies dominating at the extreme east of the basin. The former agree quite well with Oberhuber's climatology (not shown), although agreement is poor at the extreme east of the basin. The annual cycle in shortwave radiation at the equator reflects the effects of cloud. Near 90°W, the model fails to capture the observed negative shortwave anomalies that accompany the cold tongue and are associated with PBL stratus. In the cold phase of SST, the model also fails to reproduce a concurrent positive evaporation anomaly associated with a positive wind-speed anomaly in the observed data (not

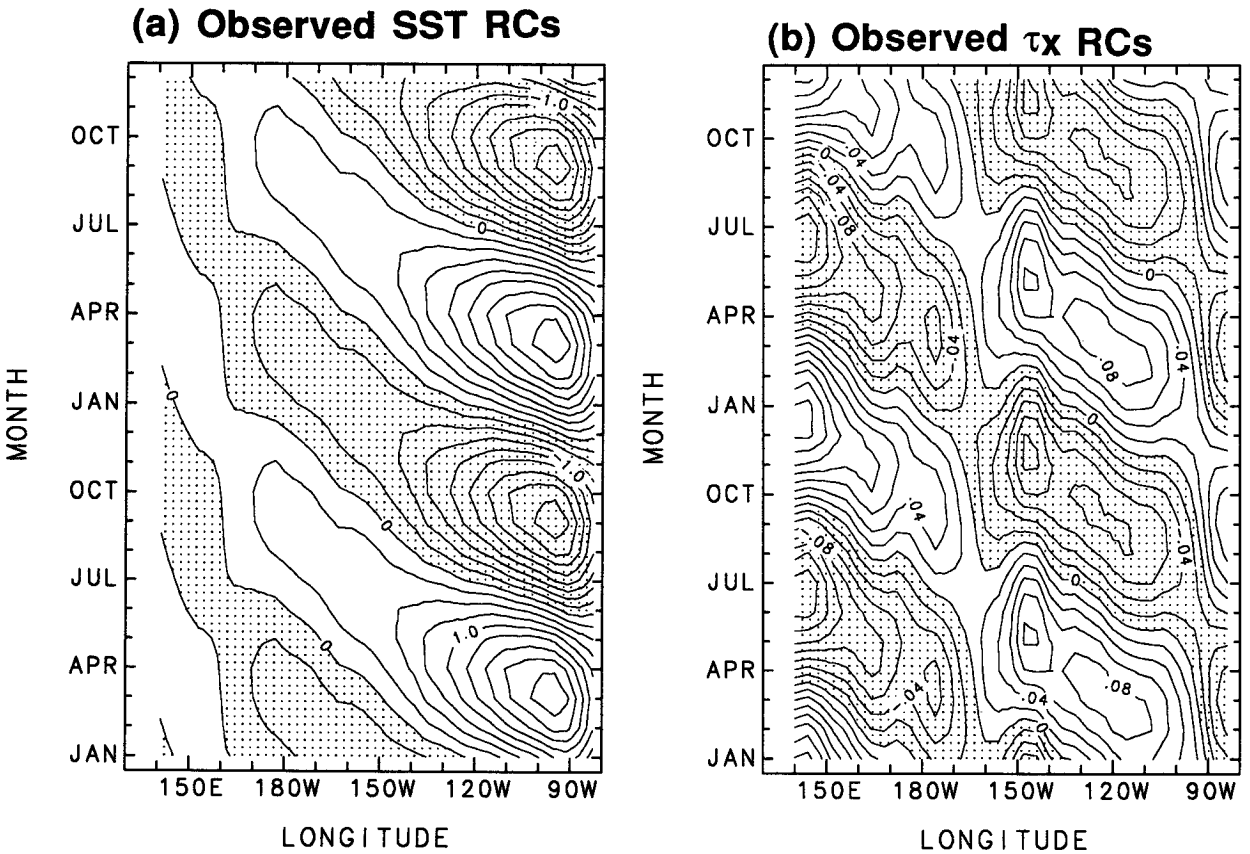

FIG. 13. Observed annual cycle RCs—(a) SST (NMC; as in Fig. 6) (0.25 K) and (b) zonal wind stress (FSU; as in Fig. 3) (0.02 dyn cm^{-2}). As in Fig. 12.

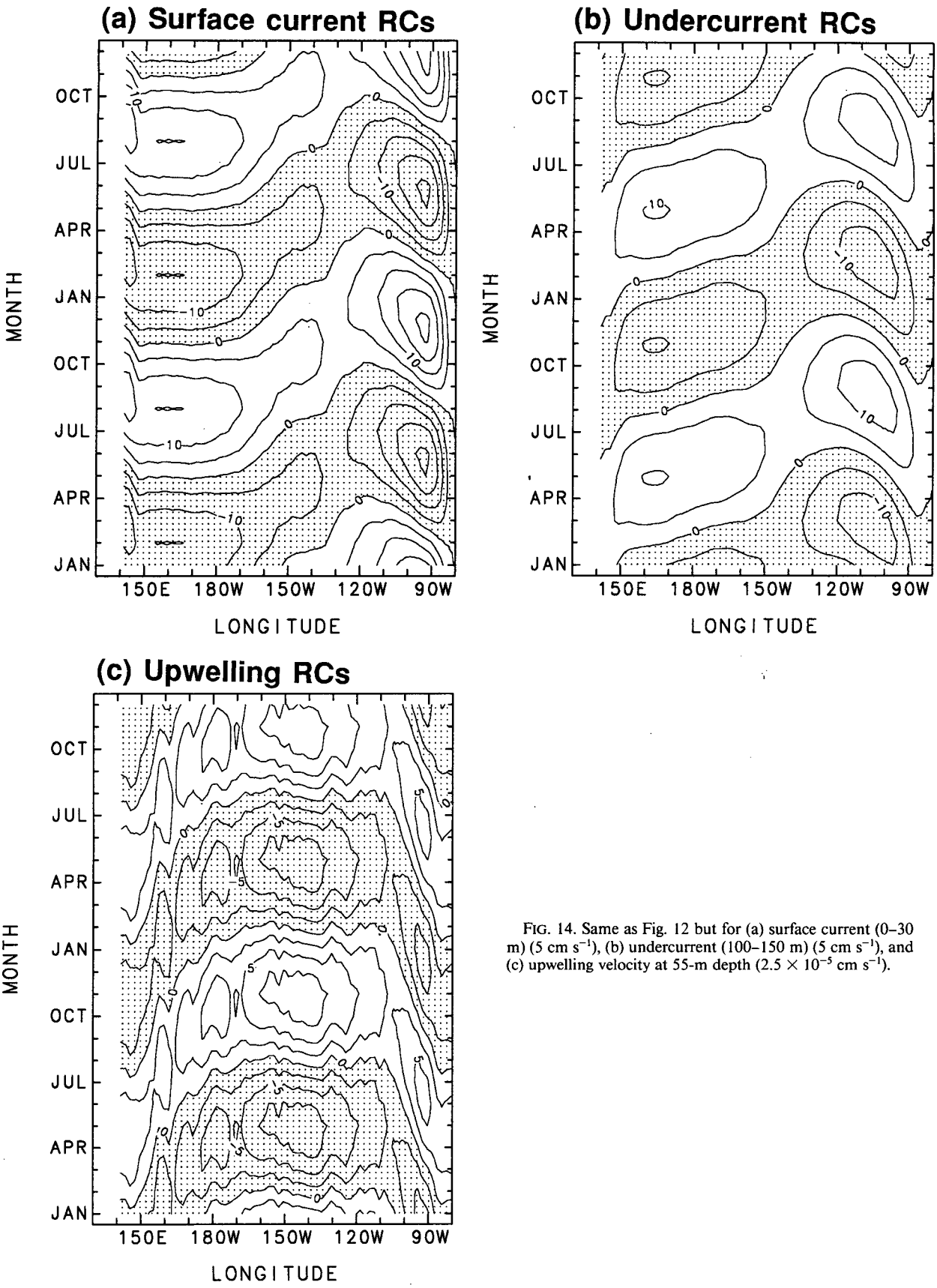

FIG. 14. Same as Fig. 12 but for (a) surface current (0–30 m) (5 cm s^{-1}), (b) undercurrent (100–150 m) (5 cm s^{-1}), and (c) upwelling velocity at 55-m depth (2.5 × 10^{-5} cm s^{-1}).

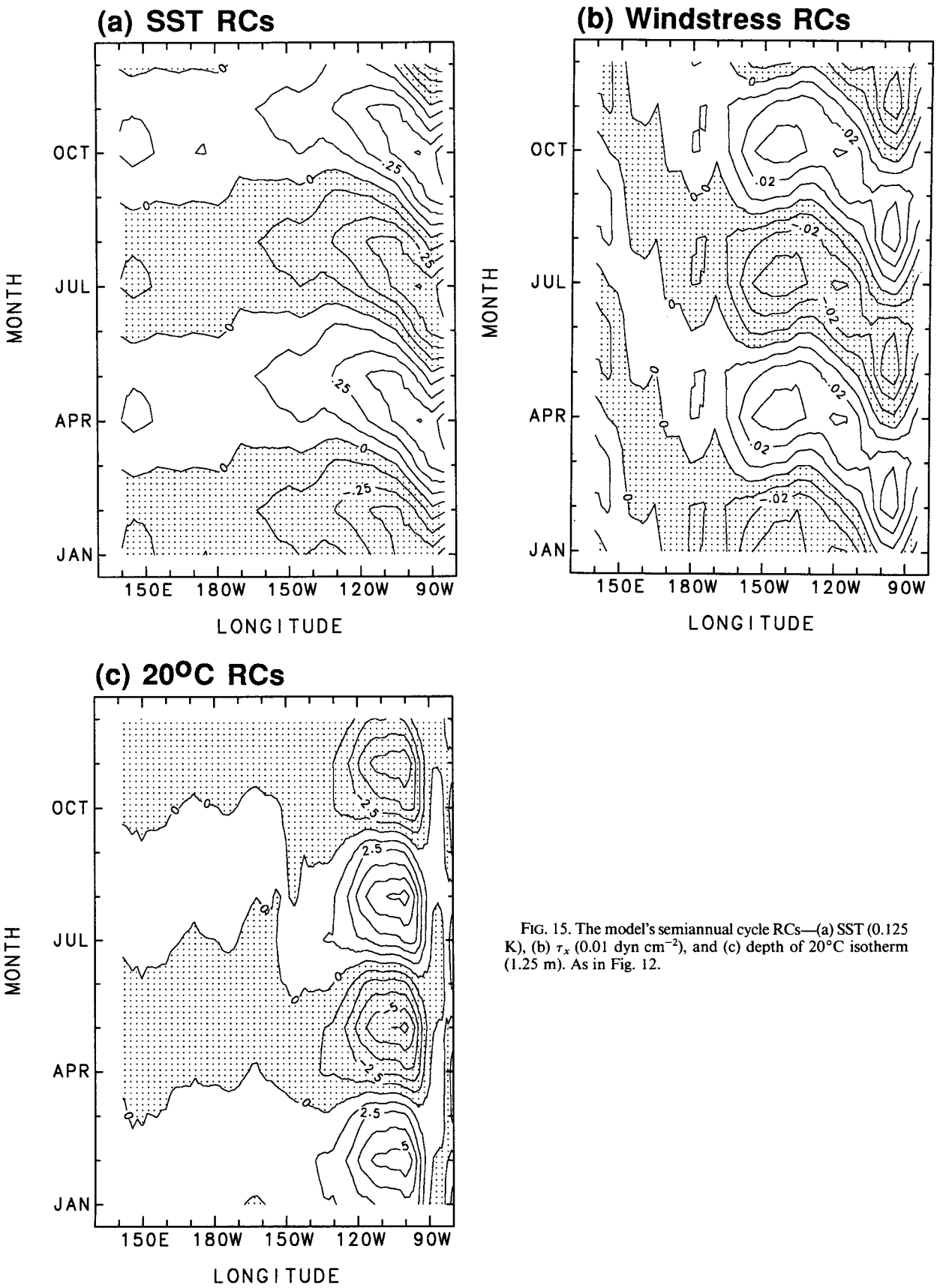

FIG. 15. The model's semiannual cycle RCs—(a) SST (0.125 K), (b) τ_x (0.01 dyn cm^{-2}), and (c) depth of 20°C isotherm (1.25 m). As in Fig. 12.

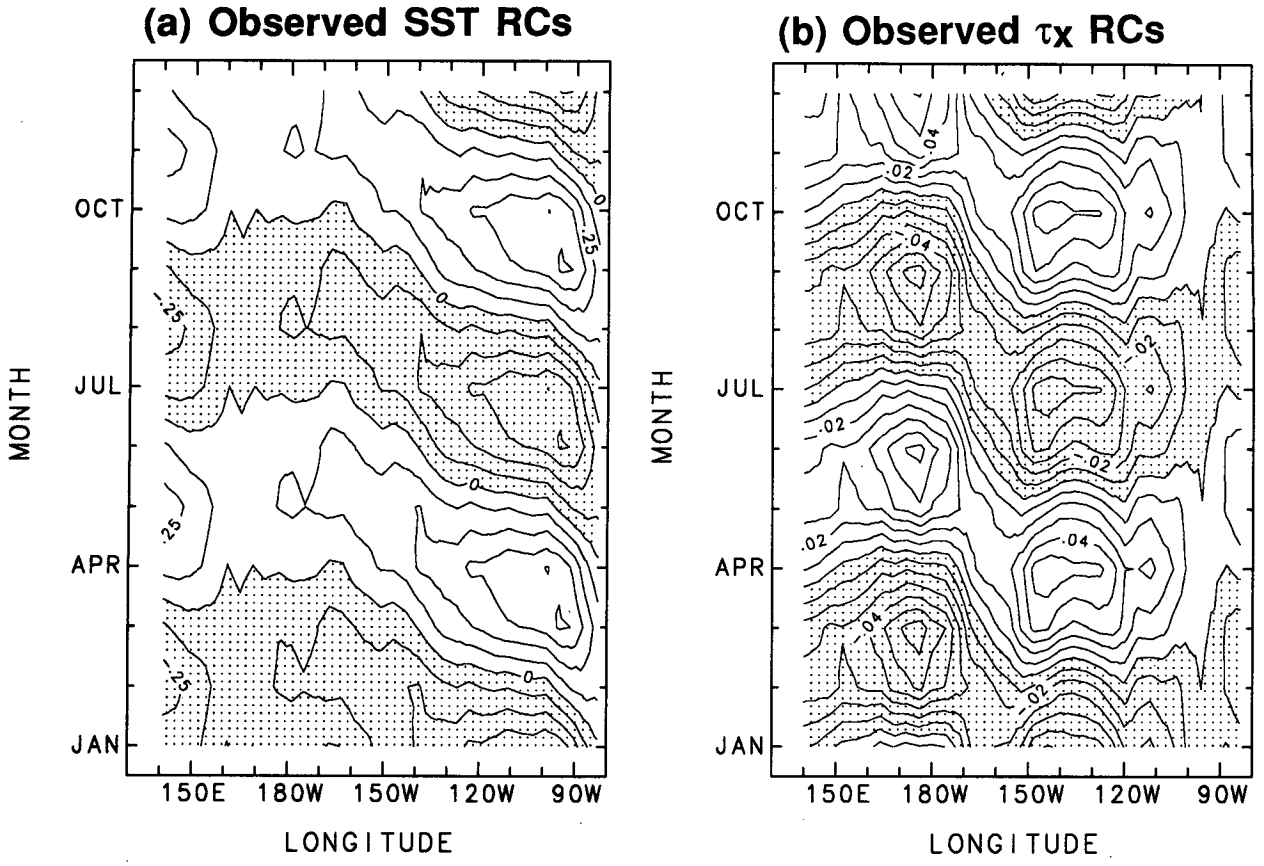

FIG. 16. Observed semiannual cycle RCs—(a) SST (NMC; as in Fig. 6) (0.125 K) and (b) zonal windstress (FSU; as in Fig. 3) (0.02 dyn cm^{-2}). As in Fig. 12.

shown). Thus, in the annual cycle, the observed net heat flux into the ocean is in phase with SST in the extreme eastern equatorial Pacific, tending to amplify the SST variation (compare Fig. 9), though the in-phase relationship does not imply a forcing. In the simulation, however, the net heat flux in this region tends to damp the annual SST cycle. This indicates that the model's seasonal cold tongue is more adiabatic than in reality.

The semiannual cycle of the net heat flux (Fig. 18) is dominated by the annual march in shortwave radiation at the surface. This is quite reasonably simulated by the model, though the amplitude of variation is somewhat underestimated.

5. Conclusions

The UCLA coupled GCM produces a realistic simulation of the mean climate and seasonal cycle over the tropical Pacific. The seasonal cold tongue in the eastern equatorial Pacific is reasonable in amplitude, extent, and duration. The model reproduces the warm pool in the west Pacific, together with its north–south migration with the season. Both the ITCZ and SPCZ are present, and the equatorial current system is reproduced by the model. The equatorial thermocline is reasonably well defined and correctly located.

There are some clear deficiencies, however, that require further work. The model SST is systematically too cold in the Tropics, with the exception of the coastal regions off Peru and California that are generally too warm. The latter deficiency may be connected with poor resolution of coastal upwelling and the associated eastern boundary currents or with deficiencies in the simulation of PBL stratus over these regions. These overestimated SSTs are associated with errors in the surface winds, which may reflect a misrepresentation of topographic effects due, at least in part, to the smooth surface elevations used in the model, or involve coupled feedbacks. The systematic coldness of SSTs across most of the tropical Pacific remains to be addressed. The model's ITCZ and SPCZ lack intensity; this lack is consistent with the cold bias, via the nonlinear dependence of deep convection on absolute SST. The atmospheric circulation, and the surface winds in particular, are also affected by the weakness of the convergence zones.

The model's surface winds are too weak along the equator, and the associated equatorial ocean currents

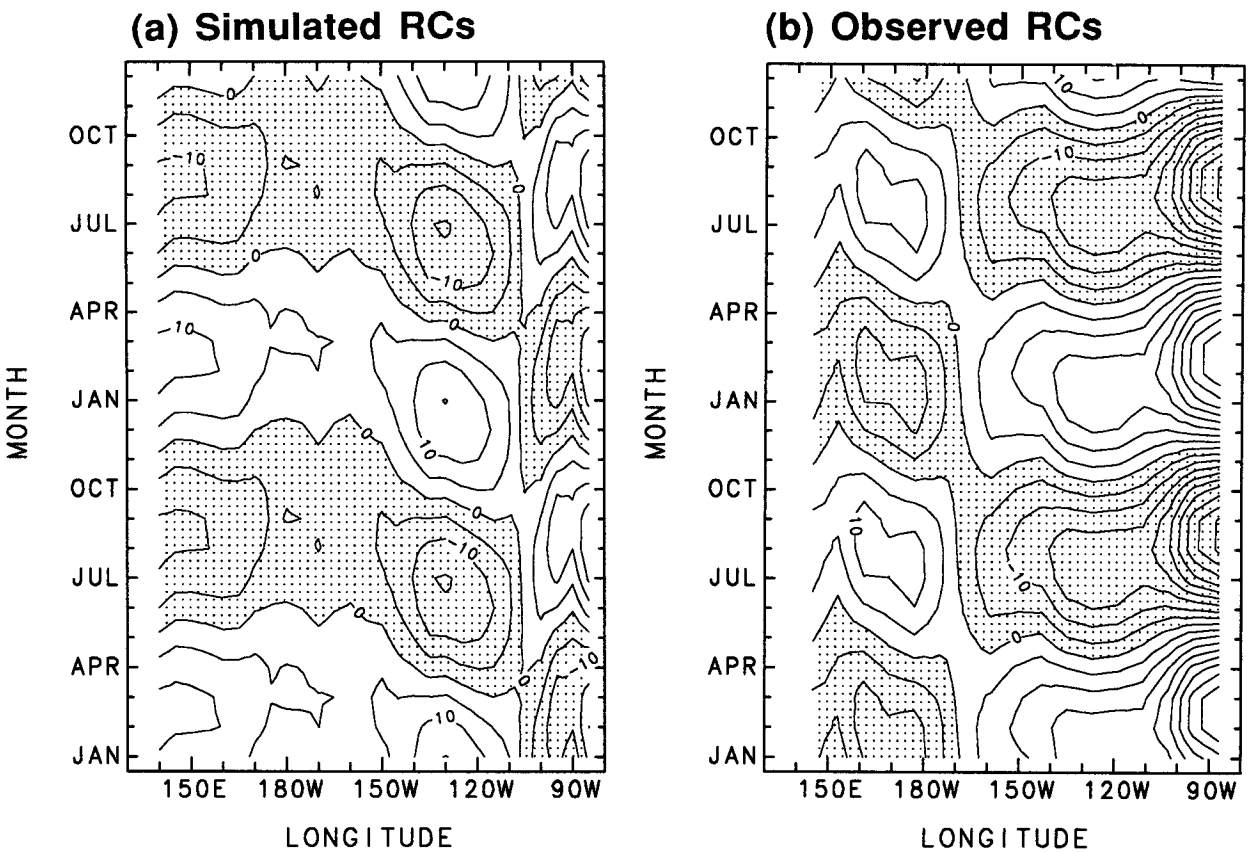

FIG. 17. The annual harmonic RCs of the net heat flux into the ocean at the equator—(a) simulated (20.0%) and (b) observed data of Oberhuber (1988) (35.1%). The contour interval is 5 W m^{-2}, and negative anomalies are stippled. The variance carried by the RC pair is given in brackets; the observed percentage is substantially higher because the analysis is based on a monthly climatology.

are thus not strong enough. Since the trade winds off the equator are quite realistic in amplitude, the problem appears to be local to the equator. A possible reason for this deficiency involves errors in the vertical mixing by low-level clouds. The mismatch in horizontal resolution between the AGCM and OGCM—largest at the equator—may also play a role. A related problem is the tendency toward a double ITCZ structure straddling the equator in the mean, with SSTs being too warm on the southern flank of the cold tongue. Satellite-derived cloud climatologies indicate that a double ITCZ structure does in fact occur in April (Waliser and Gautier 1993), and ocean–atmosphere interaction is believed to play a crucial role in this through equatorial upwelling (Charney et al. 1988). The exaggerated upwelling signature at the equator in our model is indeed consistent with the simulated double ITCZ structure.

The simulated northeast trades penetrate south of the equator in northern winter. Our current hypothesis is that this problem is at least partially due to simulation deficiencies at the eastern edge of the Pacific. The cold current provides the basic east–west asymmetry in SST and sea level pressure that prevents the ITCZ from migrating south of the equator. Lack of coastal upwelling, for the reasons given in the previous paragraph, may be connected with the model's weak Peru current. Other possible reasons for the ITCZ crossing the equator are exaggerated evaporation feedback processes associated with the southward-migrating northeast trades and lack of mixed-layer feedback at the equator. The distribution of the net heat flux into the ocean is quite well simulated except in the extreme eastern Pacific. Again, this deficiency appears to be largely associated with inadequate simulation of PBL stratus clouds.

A multichannel singular spectrum analysis (M-SSA) was used to describe the model's seasonal cycle in SST, wind stress, net surface heat flux, and ocean currents in the equatorial Pacific. The constituent annual and semiannual cycles provide a clearer picture of the march of the seasons at the equator than multiyear averages for each calendar month. The annual and semiannual cycles of SST in the eastern equatorial Pacific are well simulated by the CGCM, especially in amplitude. By contrast, the amplitudes of the annual and semiannual cycles

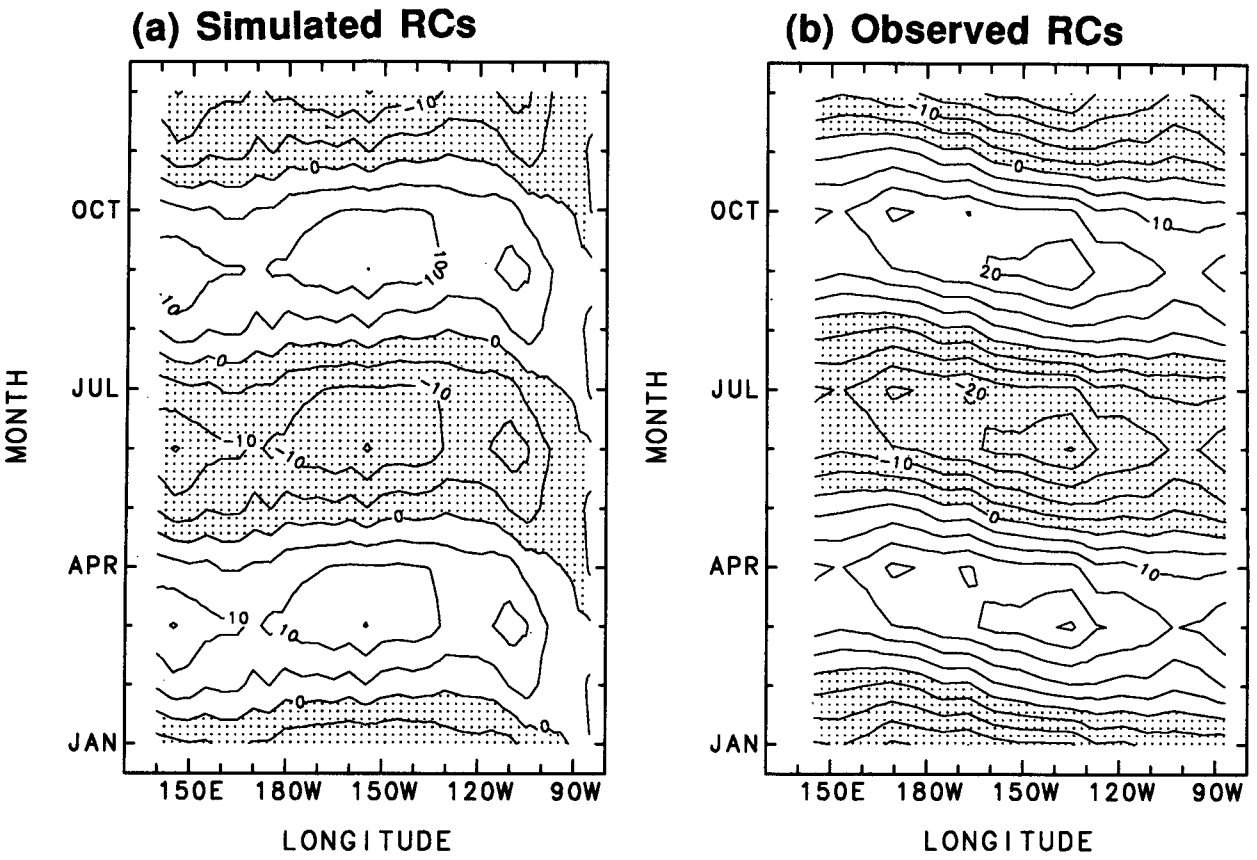

FIG. 18. The semiannual cycle RCs of the net heat flux into the ocean at the equator: (a) simulated (27.0%) and (b) observed data (60.8%). As in Fig. 17.

of the simulated zonal wind stress are both underestimated by about a factor of 2; this agrees with the model's underestimation of the climatological annual mean wind stress at the equator. The model's weak annual cycle in τ_x at the equator can be interpreted in terms of the weak coupling strength, characterized by the ratio of the τ_x anomaly to that of SST, which is underestimated by about half.

We speculate that the northeast trades are partly responsible for the realistic amplitude of the annual cycle of SST at the equator, as well as for the phase error in the latter. In northern spring, the model's northeast trades penetrate anomalously far south, even crossing the equator. Large seasonal anomalies in thermocline depth (not shown) accompany these displacements—via Ekman pumping—and it appears that these contribute to the pronounced annual cycle anomalies in equatorial thermocline depth seen in Fig. 12c. The latter—whose phase is thus partially determined by the north–south displacement of the northeast trades—affect SST via the mean upwelling.

The equatorial net heat flux acts to damp the model's SST variation at the eastern edge of the basin, mainly through evaporation. This contrasts with the observed data of Oberhuber (1988), where the flux acts to amplify the annual cycle in SST via both the effects of PBL stratus and the effects of surface winds on evaporation. This suggests that the model's cold tongue is more adiabatic in character than in reality; it appears to be largely a product of equatorial upwelling.

In contrast to the pronounced eastward propagating thermocline structure of the annual mode, the semiannual cycle has a standing thermocline structure localized near 110°W, which is consistent—via approximate Sverdrup balance—with a wind-stress signature confined to the eastern Pacific. The CGCM's semiannual cycle in SST differs accordingly from that of the annual cycle. It shows a marked westward propagation in tandem with the wind stress, which is one of the hallmarks of the "coupled SST-mode" of Neelin (1991). Here, westerly wind stress anomalies occur just to the west of the positive SST anomaly (and vice versa), thus affecting vertical motion just to the west of the latter, so that the whole set of coupled anomalies then moves westward.

In both CGCM and observed data, the semiannual cycle has a stress-to-SST anomaly ratio closer to the coupled interannual modes of Part II, which is about

four times that of the annual cycle. It is plausible that the semiannual cycle might be governed by coupled equatorial dynamics to a larger extent than the annual cycle. The annual cycle is dominated by a component that is meridionally antisymmetric about the equator, associated with the seasonal migration of the sun. The annual cycle of the equatorial wind field is thus primarily associated with the large seasonal changes in the off-equatorial mass field. In contrast, the semiannual cycle is primarily associated with the equatorial mass field.

Acknowledgments. It is a pleasure to thank A. Arakawa, Y. Chao, J. D. Farrara, F.-F. Jin, M. Latif, J. D. Neelin, and S. G. H. Philander for helpful discussions. We are grateful to J. Spahr for computing support and to N. Jiang and C. Penland for some of their computer programs. An anonymous reviewer provided many constructive comments that improved the manuscript. This work was supported by NSF and DARPA under Cooperative Agreement NCR-8919038 with CNRI (AWR, CCM, and CRM), by INCOR and "T-POP" (AWR), and by an NSF Special Creativity Award (MG). The model integrations were performed at the San Diego Supercomputer Center. The development of the model was partially supported by ONR Grant N00014-89J-1845.

REFERENCES

Arakawa, A., and W. H. Schubert, 1974: Interaction of a cumulus cloud ensemble with the large-scale environment, Part I. *J. Atmos. Sci.*, **31**, 674–701.

Broomhead, D. S., and G. P. King, 1986: Extracting qualitative dynamics from experimental data. *Physica D*, **20**, 217–236.

Bryan, K., 1969: A numerical method for the study of the circulation of the world ocean. *J. Comput. Phys.*, **4**, 347–376.

Cane, M. A., and E. S. Sarachik, 1981: The response of a linear baroclinic equatorial ocean to periodic forcing. *J. Mar. Res.*, **39**, 651–693.

——, S. E. Zebiak, and S. C. Dolan, 1986: Experimental forecasts of El Niño. *Nature*, **321**, 827–832.

Charney, J. G., E. Kalnay, E. Schneider, and J. Shukla, 1988: A study of the dynamics of the ITCZ in a symmetric atmosphere–ocean model. NASA Tech. Memor. 86220, 20 pp.

Cox, M. D., 1984: A primitive equation three-dimensional model of the ocean. GFDL Ocean Group Tech. Rep. No. 1, 143 pp.

Deardorff, J. W., 1972: Parameterization of the planetary boundary layer for use in general circulation models. *Mon. Wea. Rev.*, **100**, 93–106.

Ghil, M., and C. R. Mechoso, 1992: Data assimilation and predictability studies for the coupled ocean-atmosphere system. *Oceanogr.*, **5**, 19–24.

——, M. Kimoto, and J. D. Neelin, 1991: Nonlinear dynamics and predictability in the atmospheric sciences. *Rev. Geophys.*, (Suppl.), 46–55.

Harshvardhan, R. D., D. A. Randall, and T. G. Corsetti, 1987: A fast radiation parameterization for general circulation models. *J. Geophys. Res.*, **92**, 1009–1016.

Horel, J. D., 1982: On the annual cycle of the tropical Pacific atmosphere and ocean. *Mon. Wea. Rev.*, **110**, 1863–1878.

Jin, F.-F., J. D. Neelin, and M. Ghil, 1994: El Niño on the Devil's staircase: Annual subharmonic steps to chaos. *Science*, **264**, 70–72.

Katayama, A., 1972: A simplified scheme for computing radiative transfer in the troposphere. Numerical Simulation of Weather and Climate Tech. Rep. No. 6, Dept. of Atmospheric Sciences, University of California, Los Angeles, 77 pp.

Kimoto, M., M. Ghil, and K.-C. Mo, 1991: Spatial structure of the extratropical 40-day oscillation. *Proc. Eighth Conf. on Atmospheric and Oceanic Waves and Stability*, Denver, CO, Amer. Meteor. Soc., 115–116.

Lau, N.-C., S. G. H. Philander, and M. J. Nath, 1992: Simulation of ENSO-like phenomena with a low-resolution coupled GCM of the global ocean and atmosphere. *J. Climate*, **5**, 284–307.

Levitus, S., 1982: Climatological atlas of the world ocean. NOAA Professional Paper No. 13, 173 pp.

Ma, C.-C., C. R. Mechoso, A. Arakawa, and J. D. Farrara, 1994: Sensitivity of tropical climate in a coupled ocean-atmosphere general circulation model. *J. Climate*, **7**, 1883–1896.

Mechoso, C. R., C.-C. Ma, J. D. Farrara, and J. A. Spahr, 1991: Simulations of interannual variability with a coupled atmosphere-ocean general circulation model. Preprints, *Fifth Conf. Climate Variations*, Denver, CO, Amer. Meteor. Soc., J1–J4.

Meehl, G. A., 1987: The annual cycle and its relationship to interannual variability in the tropical Pacific and Indian Ocean regions. *Mon. Wea. Rev.*, **115**, 27–50.

——, 1990: Seasonal cycle forcing of El Niño–Southern Oscillation in a global coupled ocean–atmosphere GCM. *J. Climate*, **3**, 72–98.

Mellor, G. L., and T. Yamada, 1982: Development of a turbulence closure model for geophysical fluid problems. *Rev. Geophys. Space Phys.*, **20**, 851–875.

Meyers, G., 1979: Annual variation in the slope of the 14°C isotherm along the equator in the Pacific Ocean. *J. Phys. Oceanogr.*, **9**, 885–891.

Neelin, J. D., 1991: The slow sea surface temperature mode and the fast-wave limit: Analytic theory for tropical interannual oscillations and experiments in a hybrid coupled model. *J. Atmos. Sci.*, **48**, 584–606.

——, F.-F. Jin, and M. Latif, 1994: Dynamics of coupled ocean-atmosphere models: The tropical problem. *Ann. Rev. Fluid Mech.*, **26**, 617–659.

Oberhuber, J. M., 1988: An atlas based on the COADS data set: The budgets of heat buoyancy and turbulent kinetic energy at the surface of the global ocean. Max Planck Institut für Meteorologie Report No. 15, Hamburg, 20 pp.

Pacanowski, R. C., and S. G. H. Philander, 1981: Parameterization of vertical mixing in numerical models of tropical oceans. *J. Phys. Oceanogr.*, **11**, 1443–1451.

Philander, S. G. H., 1978: Instabilities of zonal currents, Part II. *J. Geophys. Res.*, **83**, 3679–3682.

——, and Y. Chao, 1991: On the contrast between the seasonal cycles of the equatorial Atlantic and Pacific oceans. *J. Phys. Oceanogr.*, **21**, 1399–1406.

——, W. J. Hurlin, and A. D. Seigel, 1987: Simulation of the seasonal cycle of the tropical Pacific ocean. *J. Phys. Oceanogr.*, **17**, 1986–2002.

——, R. C. Pacanowski, N.-C. Lau, and M. J. Nath, 1992: Simulation of ENSO with a global atmospheric GCM coupled to a high-resolution tropical Pacific ocean GCM. *J. Climate*, **5**, 308–329.

Plaut, G., and R. Vautard, 1993: Spells of low-frequency oscillations and weather regimes in the Northern Hemisphere. *J. Atmos. Sci.*, **51**, 210–236.

Reynolds, R. W., 1988: A real-time global sea surface temperature analysis. *J. Climate*, **1**, 75–86.

Robertson, A. W., C.-C. Ma, C. R. Mechoso, and M. Ghil, 1994: Simulation of the tropical Pacific climate with a coupled ocean–

atmosphere general circulation model. Part II: Interannual variability. *J. Climate,* **8,** 1199–1216.

Stricherz, J. N., J. J. O'Brien, and D. M. Legler, 1992: Atlas of Florida State University tropical Pacific winds for TOGA 1966–1985. Mesoscale Air–Sea Interaction Group Tech. Rep., Florida State University, 4 pp.

Suarez, M. J., A. Arakawa, and D. A. Randall, 1983: The parameterization of the planetary boundary layer in the UCLA general circulation model: Formulation and results. *Mon. Wea. Rev.,* **111,** 2224–2243.

Tziperman, E., L. Stone, H. Jarosh, and M. A. Cane, 1994: El Niño chaos: Overlapping of resonances between the seasonal cycle and the Pacific ocean–atmosphere oscillator. *Science,* **264,** 72–74.

Vautard, R., and M. Ghil, 1989: Singular spectrum analysis in nonlinear dynamics with applications to paleoclimatic time series. *Physica D,* **35,** 395–424.

——, P. Yiou, and M. Ghil, 1992: Singular-spectrum analysis: A toolkit for short, noisy chaotic signals. *Physica D,* **58,** 95–126.

Waliser, D. E., and C. Gautier, 1993: A satellite-derived climatology of the ITCZ. *J. Climate.,* **6,** 2162–2174.

Weare, B. C., and J. S. Nasstrom, 1982: Examples of extended empirical orthogonal function analyses. *Mon. Wea. Rev.,* **110,** 481–485.

Zebiak, S. E., and M. A. Cane, 1987: A model El Niño Southern Oscillation. *Mon. Wea. Rev.,* **115,** 2262–2278.